UC San Diego
UC San Diego Previously Published Works

Title

Multicompartment imaging of the brain using a comprehensive MR imaging protocol.

Permalink

https://escholarship.org/uc/item/0v15f3tb

Authors

Lo, James

Du, Kevin

Lee, David

et al.

Publication Date

2024-09-01

DOI

10.1016/j.neuroimage.2024.120800

Peer reviewed

Multicompartment Imaging of the Brain Using a Comprehensive MR Imaging Protocol

James Lo[1,2], **Kevin Du**[1], **David Lee**[1], **Chun Zeng**[1], **Jiyo S. Athertya**[1], **Melissa Lou Silva**[1], **Reese Flechner**[1,3], **Graeme M. Bydder**[1], **Yajun Ma**[1]

[1]Department of Radiology, University of California, San Diego, CA, USA

[2]Department of Bioengineering, University of California, San Diego, CA, USA

[3]Department of Biomedical Engineering, Vanderbilt University, Nashville, TN, USA

Abstract

In this study, we describe a comprehensive 3D magnetic resonance imaging (MRI) protocol designed to assess major tissue and fluid components in the brain. The protocol comprises four different sequences: 1) magnetization transfer prepared Cones (MT-Cones) for two-pool MT modeling to quantify macromolecular content; 2) short-TR adiabatic inversion-recovery prepared Cones (STAIR-Cones) for myelin water imaging; 3) proton-density weighted Cones (PDw-Cones) for total water imaging; and 4) highly T_2 weighted Cones (T_2w-Cones) for free water imaging. By integrating these techniques, we successfully mapped key brain components —namely macromolecules, myelin water, intra/extracellular water, and free water—in ten healthy volunteers and five patients with multiple sclerosis (MS) using a 3T clinical scanner. Brain macromolecular proton fraction (MMPF), myelin water proton fraction (MWPF), intra/extracellular water proton fraction (IEWPF), and free water proton fraction (FWPF) values were generated in white matter (WM), grey matter (GM), and MS lesions. Excellent repeatability of the protocol was demonstrated with high intra-class correlation coefficient (ICC) values. In MS patients, the MMPF and MWPF values of the lesions and normal-appearing WM (NAWM) were significantly lower than those in normal WM (NWM) in healthy volunteers. Moreover, we observed significantly higher FWPF values in MS lesions compared to those in NWM and NAWM regions. This study demonstrates the capability of our technique to volumetrically map major brain components. The technique may have particular value in providing a comprehensive assessment of neuroinflammatory and neurodegenerative diseases of the brain.

Corresponding Author: Yajun Ma, Ph.D., yam013@ucsd.edu, University of California San Diego, Department of Radiology, 9452 Medical Center Drive, La Jolla, CA 92037.

1. Introduction

The brain is a complex organ that contains four main tissue and fluid compartments, namely motion-restricted macromolecules (MM) (e.g., myelin lipid, myelin basic protein, and axonal membranes with ultrashort T_2s of ~10μs), myelin water (MW) (i.e., water trapped in the myelin lipid layers with T_2s of ~10ms), intracellular/extracellular water (IEW) (i.e., water semi-restricted within cell cytoplasm and the intercellular space with T_2s ~40–90ms), and free water (FW) (e.g., unrestricted cerebrospinal fluid (CSF) in the subarachnoid space and ventricular system with T_2s longer than 1000ms)[1–6]. Compositional changes in these components occur in many neuroinflammatory and neurodegenerative diseases, such as multiple sclerosis (MS)[1–6].

Magnetic resonance imaging (MRI) has emerged as a critical tool in clinical and research settings due in large part to significant disease-dependent changes in the T_1s and T_2s of tissue and fluid components in the brain[7–10]. However, clinical T_1- or T_2-weighted sequences have difficulty distinguishing between pathological processes in lesions such as edema, gliosis, inflammation, demyelination, and remyelination, as well as studying the effects of these pathological processes within each compartment[11]. For example, brain lesions typically appear high signal when imaged with clinical T_2-weighted sequences[12]. This lack of specificity of current clinical sequences limits the value of MRI in disease diagnosis and progression tracking, as well as in treatment monitoring. To address this problem, a variety of new MRI techniques have been developed to assess each specific brain compartment (i.e., MM, MW, IEW, and FW) and investigate their respective roles in neurodegeneration and other conditions[1–6].

For example, quantitative two-pool magnetization transfer (MT) modeling techniques have been developed to provide indirect assessment of the macromolecular content of the brain[1,2]. These techniques are based on the magnetization exchange between motion-restricted protons in semisolid compartments and mobile protons in liquid compartments. The techniques have proven useful in differentiating normal white matter (NWM) in healthy individuals from normal appearing WM (NAWM), and lesions in MS patients[1,13]. Recently, we have developed a 3D MT-prepared Cones (MT-Cones) sequence with multispoke acquisition for fast volumetric quantification of tissue macromolecular proton fraction (MMPF)[14]. A center-out spiral readout was used in the Cones acquisition[15]. In that study, a modified rectangular pulse (RP) approximation was shown to be more reliable than the typical continuous wave power equivalent (CWPE) model in multispoke acquisitions for MMPF estimation[14,16].

To assess myelin content changes in the brain, several state-of-the-art MW imaging techniques such as multi-compartment T_2/T_2^* relaxation measurements and visualization of short transverse relaxation time components (ViSTa) have been developed over the last two decades[3,4,17–20]. The multi-compartment T_2/T_2^* relaxation approach models brain tissue with two or more water compartments and separates them by postprocessing based on their T_2 or T_2^* differences[19,21]. In comparison, ViSTa selectively images the short T_1 component (i.e., MW) using a double inversion recovery (DIR) technique without complicated modeling and intensive postprocessing[18,22]. These techniques have proven sensitive to myelin loss in

MS patient studies[4,18,22,23]. Most recently, we have developed a 3D short repetition time adiabatic inversion recovery (STAIR) prepared Cones (STAIR-Cones) sequence for selective volumetric MW imaging and quantification[24]. The short TR used in the STAIR-Cones sequence provides robust signal suppression of all long T_2 water components (including IEW and FW). In comparison to ViSTa, the STAIR sequence is more time efficient because of its much shorter TR.

Brain IEW contents are typically imaged using T_2-weighted and fluid-attenuated inversion recovery (T_2-FLAIR) sequences in the clinical diagnosis of MS[25,26]. Within the T_2-FLAIR sequence, an inversion recovery (IR) pulse is applied to suppress the CSF signal, followed by a fast spin echo acquisition with a relatively long (e.g., 80–120 ms) echo time (TE) to selectively image IEW components, with the short T_2 MM and MW signals fully decayed. Hyperintense MS lesions seen on T_2-FLAIR images often appear ovular, particularly in the periventricular and juxtacortical regions[27,28].

Highly $T_{1\rho}$- and T_2-weighted sequences have been developed for selective FW imaging[5,6,29]. These sequences can detect CSF volume changes during brain activation. Very long spin-lock times or TEs are used in these $T_{1\rho}$- and T_2-weighted sequences to selectively image long $T_{1\rho}/T_2$ fluid signals. With this approach, signals from other brain components, such as MW and IEW, which have much shorter $T_{1\rho}/T_2$ relaxation times, completely decay and so are not detected. These types of sequences can be useful in the detection of longitudinal changes in CSF flow dynamics as well as in tracking volume changes in fluid within lesions during disease progression[30–32].

As described above, many novel techniques have been developed for the assessment of specific brain compartments, and these may improve current approaches used in clinical diagnosis and treatment monitoring[33–39]. Recent studies have aimed to more accurately model the relaxation dynamics and exchange processes to disentangle individual compartments in biological tissue systems[33,34,39]. For example, Assländer et al. successfully separated the T_1s of free and semi-solid pools using an unconstrained MT model and hybrid state encoding[34]. Soustelle et al. incorporated on-resonance saturation and dipolar order contributions into the traditional two-pool MT model to remove relevant biases[39]. Manning et al. utilized a four-pool model to characterize the aqueous and non-aqueous components in ex vivo bovine white matter[33].

However, to the best of our knowledge, there is no complete set of 3D protocols available to image and quantify the major tissue and fluid components of the brain in vivo. Such a protocol could be of considerable value in providing a comprehensive assessment of compositional changes in neuroinflammatory and neurodegenerative disease as well as monitoring therapeutic efficacy. To achieve this goal, we have developed a protocol using four different sequences: a MT-Cones sequence combined with two-pool MT modeling for MM content estimation[14], a STAIR-Cones sequence for MW imaging[24], a proton density-weighted Cones (PDw-Cones) sequence for total water (TW) imaging[24], and a highly T_2-weighted Cones (T_2w-Cones) sequence for FW imaging. A 3D Cones acquisition with a short TE (i.e., 0.8–2 ms) is used with each sequence, with signal weighting driven by each respective preparation module[31,32]. By combining the four sequences, we can estimate the

proton fractions (PFs) of all the major compartments in the brain (i.e., MMs, MW, IEW, and FW). Ten healthy volunteers and five patients with MS were recruited and scanned on a clinical 3T MRI scanner to assess the technique's feasibility.

2. Methods and Materials

2.1. Imaging sequences

Figure 1 shows the key features of the four sequences in the comprehensive protocol: MT-Cones, STAIR-Cones, T_2w-Cones, and PDw-Cones. A Fermi-shaped MT pulse is employed in the MT-Cones sequence to generate MT contrast followed by multispoke Cones data acquisition to speed up the scan. A series of MT-Cones data are acquired with different MT powers and frequency offsets. In addition, brain T_1 values are measured by the recently developed actual flip angle and variable flip angle Cones (AFI-VFA-Cones) technique (sequence diagrams not shown) as an input for two-pool MT modeling[40]. The modified RP MT modeling process is then used to quantify the macromolecular proton fraction (MMPF)[14]. The total water proton fraction (TWPF) is calculated as 1-MMPF.

With the STAIR-Cones sequence, an adiabatic full passage (AFP) pulse is utilized to invert the longitudinal magnetization of water components without significant compromise due to system B_0 and B_1 inhomogeneities, and this is followed by multispoke Cones data acquisition[24]. Using a sufficiently short TR (i.e., 250 ms) in conjunction with an optimal inversion time (TI) in the STAIR-Cones sequence enables the suppression of signals from long T_2 water components such as IEW and FW with a wide range of T_1s, allowing selective imaging of the fast-recovering short T_1 MW (essentially acting as a T_1 filter)[24]. Additionally, MW has a relatively short T_2 relaxation time (~10ms). The longitudinal magnetization of MW is partially inverted by the relatively long AFP pulse (duration=8.64ms), allowing more signal recovery from MW during TI in STAIR-Cones[24].

The highly T_2 weighted-Cones sequence (T_2w-Cones) includes four major features[41]: (i) a magnetization reset module to generate a constant magnetization recovery, (ii) a T_2 preparation module with a long free decay time (e.g., 350 ms), (iii) a radio frequency (RF) cycling scheme (i.e., the RF phase of the second 90° pulse in the T_2 preparation alternates by 180° in adjacent TRs), and (iv) a variable flip angle (VFA) technique to reduce signal variation along the multispoke data acquisition and improve the signal-to-noise ratio (SNR) performance of the sequence for acquisition of FW signal.

The PDw-Cones sequence is utilized for fast TW imaging. It employs a relatively low flip angle (e.g., 1°) for signal excitation and reduction of T_1-weighting. A 3D AFI-Cones sequence was utilized to map and correct B_1 inhomogeneity in the MT modeling[40].

In each acquisition spoke of the above sequences, a slab-selective RF pulse is utilized for signal excitation followed by center-out spiral encoding. This spiral encoding forms a 3D Cones trajectory which covers the whole of k-space efficiently[42].

2.2. Multicompartment mapping

The workflow to calculate the MM, MW, IEW, and FW PFs (i.e., MMPF, MWPF, IEWPF, and FWPF) in the brain is illustrated in Figure 2.

The MW, TW, and FW images are directly generated by the STAIR-Cones, PDw-Cones, and highly T_2w-Cones scans, respectively. The MWF, defined as the content ratio between MW and TW, is calculated using Eq. [13] in Ref. 24, taking into account the mixed T_1 and T_2* weighting terms from the STAIR-Cones and PDw-Cones sequences. The FWF, defined as the content ratio between FW and TW, is calculated in two steps. First, the signal ratio between the highly T_2w-Cones and PDw-Cones is determined. Then, since the FWF in the ventricular region should be 1, the FWF is estimated by normalizing the signal ratio map to the signal ratio from the ventricular region. This normalization step successfully eliminates the mixed T_1, T_2*, or T_2 weighting terms from the highly T_2w-Cones and PDw-Cones sequences.

With known MWF and FWF, the IEWF, defined as the content ratio between IEW and TW, can easily be obtained using:

$$IEWF = 1 - MWF - FWF,$$

[1]

with

$$MWF = \frac{MW}{TW} \quad \text{and} \quad FWF = \frac{FW}{TW}.$$

The MMPF is directly obtained by two-pool MT modeling of a series of MT-Cones data[14]. The TWPF can be easily calculated by 1- MMPF, which is defined as the ratio of TW to total proton content (i.e., TW + macromolecular proton (MMP)):

$$TWPF = \frac{TW}{TW + MMP}.$$

[2]

Finally, with known values of MWF, FWF, and IEWF as well as TWPF, the MWPF, FWPF and IEWPF are easily obtained:

$$MWPF = MWF * TWPF,$$

[3]

$$FWPF = FWF * TWPF,$$

[4]

$$IEWPF = IEWF * TWPF.$$

[5]

2.3. MR Data Acquisition

In this study, ten healthy volunteers (aged 27±2 years old, six females) and five patients with MS (aged 55±11 years old, four females) were recruited and scanned. Written informed consent was obtained from each participant as approved by the institutional review board (IRB) of the University of California, San Diego, with registration number 201647. All participants underwent scanning with a 3T clinical scanner (MR750; GE Healthcare, Milwaukee, Wis), utilizing an 8-channel receive-only head coil for signal reception. The protocol's repeatability was assessed by scanning two healthy volunteers a total of three times each on different days. Table 1 provides detailed sequence parameters used in this study.

2.4. Data Analysis

Image registration was used to align all the acquired data for each volunteer using Elastix[43]. Multicompartment mapping was carried out using MATLAB software (Mathworks Inc., Natick, Mass). Regions of interest (ROIs) were manually delineated in eight WM regions and two grey matter (GM) regions by a neuroradiologist with 15 years' experience i.e., the left and right centrum semiovales, periventricular regions, subcortical white matter, the splenium and genu of the corpus callosum (WM) as well as the putamen and thalamus (GM). Additional ROIs were drawn in lesions in each of the MS patients. The lesions were identified and localized with T_2-FLAIR images.

Intra-class correlation coefficients (ICCs) were calculated to demonstrate the repeatability of the protocol using SPSS software (IBM, Armonk, NY, USA). Ten ROIs (i.e., eight WM and two GM as described above) were delineated on the first scan of each subject and these ROIs were applied to their second and third scans to obtain their corresponding positions.

An independent t-test was conducted for the PFs of NWM, NAWM, normal GM (NGM), normal appearing GM (NAGM), as well as lesions comparing normal volunteer and MS groups. The PFs of MS lesions were compared with those of both NAWM and NWM. A p-value less than 0.05 was considered statistically significant.

3. Results

3.1 Multicompartment brain images

Figure 3 shows representative MT-, PDw-, STAIR-, and highly T_2w-Cones images acquired from a healthy volunteer. Greater MT contrast is evident in the images with higher MT FA and lower frequency offset MT-Cones. The STAIR-Cones images reveal a higher concentration of MW in WM regions than in GM regions. In the highly T_2w-Cones images, the extended T_2 preparation time (i.e., 350 ms) ensures complete decay of signals from MM, MW, and IEW (which have relatively short T_2s) while retaining signals from long T_2 CSF.

3.2 Proton fraction maps

Figure 4 shows MMPF, MWPF, IEWPF, and FWPF maps obtained from the same healthy volunteer featured in Figure 3. In WM, the MMPF, MWPF, and IEWPF range from 10 to 12%, 7 to 9%, and 75 to 79%, respectively. In GM, the MMPF, MWPF, and IEWPF range from 4 to 7%, 1.5 to 3%, and 83 to 89%, respectively. Notably, WM exhibits much higher MMPF and MWPF values than GM, whereas GM demonstrates higher IEWPF values than WM. FW is predominantly present in the ventricles and subarachnoid space, and is largely absent from both WM and GM regions in a normal brain, with FWPF in both WM and GM ranging from 0 to 4%.

3.3. Scan repeatability

The repeatability analysis of the three scans done in each volunteer shows high ICC values for MMPF, MWPF, IEWPF, and FWPF measurements (Subject 1: 0.98, 0.98, 0.98, and 0.88, respectively; Subject 2: 0.99, 0.99, 0.99, and 0.90, respectively), indicating excellent repeatability of the comprehensive protocol.

3.4. Comparison between normal volunteers and MS patients

Figure 5 depicts PF maps acquired from a normal volunteer and three patients diagnosed with MS. Lesions were identified using T_2-FLAIR images. They are absent in the normal group but display their characteristic hyperintensities in the MS group. Lesions are distinguishable from surrounding ventricular, WM, and GM regions in all PF maps (highlighted by yellow arrows). They appear as hypointensities on the MMPF, IEWPF, and MWPF maps. Notably, on the FWPF map, lesions show mild hyperintensities, albeit less intense than FW within the ventricular region.

Figure 6 depicts bar plots illustrating MMPF, MWPF, IEWPF, and FWPF measurements for the ten normal volunteers and five patients with MS. MMPF and MWPF measurements in relatively normal WM matter regions (i.e., NWM and NAWM) are notably higher than those in GM regions in both healthy volunteers and MS patients, consistent with WM's higher myelin content compared to GM. Moreover, significant differences in all four measurements, including MMPF, MWPF, IEWPF, and FWPF, are seen between NWM and NAWM, NWM and lesions, and NAWM and lesions. Significant differences between NGM and NAGM measurements are seen only in IEWPF and FWPF, but not in MMPF and MWPF. The MMPF, MWPF, IEWPF, and FWPF measurements for the normal volunteers and MS patients are summarized in Table 2.

4. Discussion

In this study, we explored the feasibility of a comprehensive multicompartment imaging protocol for assessing brain composition in normal volunteers and patients with MS. Our protocol, which incorporates MT-, PDw-, STAIR-, and T_2w-Cones sequences, effectively mapped the PFs of WM, GM, and lesion regions across four key compartments (i.e., macromolecules, MW, IEW, and FW) of the brain. Significant differences were observed in MMPF and MWPF maps between NWM and NAWM, as well as between lesions and relatively normal WM regions. Moreover, distinct differences were found between NGM and

NAGM values in IEWPF and FWPF maps. FWPFs in lesions and NAWM were higher than those in NWM. These findings demonstrate the technical feasibility of the protocol and its promise in clinical use.

Neuroinflammatory and neurodegenerative diseases often manifest their pathological progression through compositional alterations[1–6,44–46]. Particularly in MS, focal lesions, diffuse damage to myelin sheaths and axons, and the replacement of tissue by CSF are prominent features[47–50]. Our technique shows that in MS patients, lesion MMPF, MWPF, and IEWPF values are notably lower than those observed in WM and GM regions in both normal volunteer and MS groups. Despite being localized in WM areas, lesion PFs closely resemble those of GM, indicating a significant degradation of myelin structure.

The MMPFs of NAWM are significantly lower than those of NWM, consistent with findings in previous neuropathological studies[51–53]. The decrease in MM content in WM lesions may stem from neurodegeneration. The changes in lesions may be associated with pathological and inflammatory alterations around them, leading to adjacent NWM transitioning into NAWM[54].

NAWM shows a significant decrease in MWPF compared to NWM, while lesions have notably lower MWPF than both NWM and NAWM. This phenomenon may arise from diffuse neurodegeneration in MS brains, causing tissues adjacent to lesions to exhibit behavior akin to NAWM[48]. These findings are consistent with prior studies demonstrating a widespread reduction in MWF of NAWM in MS patients compared to normal volunteers, with further decreases observed as the disease progresses[4,53,55,56].

Significant differences are observed in IEWPF measurements between NWM and NAWM, NWM and lesions, as well as between NAWM and lesions. These findings are consistent with prior research indicating an elevated level of extracellular water in MS patients compared to normal volunteers, possibly due to the breakdown of structural barriers affecting water motion[46,57,58]. The considerably lower IEWPFs in MS lesions compared to NAWM may reflect structural damage. It is noteworthy that while clinically utilized T_2-FLAIR relies primarily on the T_2 contrast of the IEW for diagnosis, our study maps the PF of IEW.

Both WM and GM regions exhibit relatively low FWPFs in both the normal volunteer and MS groups, as free water predominantly occupies non-WM or GM regions, such as the ventricular system and subarachnoid space. Recent studies on MS lesions have demonstrated a transition in volume from lesion to CSF due to atrophy or lesion destruction[49,50]. This finding is reflected in our results, where lesion FWPF measurements are significantly and markedly higher than those of both WM and GM in both groups. Moreover, FWPF measurements of NAWM and NAGM are significantly higher than those of the corresponding regions in NWM and NGM, respectively. This may be attributed to the aforementioned diffuse neurodegeneration and requires validation in future studies. The overall increase in FW content in MS brains may have implications for the interplay between different compartments throughout the course of disease progression.

Quantitative MRI combined with biophysical models, termed in vivo histology using MRI (hMRI), has become an attractive technology for non-invasively obtaining structural and compositional information[35]. However, biological tissue systems are very complex, consisting of various types of macromolecules and the environments these macromolecules create for water molecules. This results in different cohorts of water components, each with distinct MRI properties. Therefore, a multicompartment model should be considered to more accurately describe the tissue system. This complexity is further heightened by multiple exchange processes between these macromolecular and water pools, including MT, chemical exchange saturation transfer, and diffusion[33–35,39].

Conventional MRI cannot directly detect signals from macromolecules due to their ultrashort T_2s (~10μs). To address this, MT modeling techniques have been developed to indirectly assess structural and compositional changes of macromolecular components in tissues[59]. The two-pool MT model is the most simplified and widely used due to its practicality and reproducibility[59,60]. In this study, we employed a classic two-pool MT model with RP approximation, developed by Sled et al.[61], to estimate the MMPF in the brain. Our results are in good agreement with previous studies[1]. More recently, researchers have been working hard to address potential biases in traditional MT modeling techniques by incorporating B_1 inhomogeneity correction or expanding the model to include unconstrained T_1 relaxation times and considering contributions from on-resonance saturation and dipolar order[34,39]. These efforts have successfully improved the accuracy of biological tissue characterization. We expect our proposed multicompartment imaging method to deliver a more reliable estimation of modeling parameters if we incorporate all these improvements into our two-pool MT modeling process.

Exchange processes also play a significant role in non-MT sequences, such as inversion recovery (IR) sequences[33]. A recent ex vivo bovine white matter modeling study found that a bi-component model was required to fit the data acquired by the IR preparation and soft pulse excitation, while a single-component model was sufficient to fit the data with hard pulse excitation[33]. A four-pool model considering intercompartment exchange successfully characterized the white matter tissue system and explained the signal behavior for the different types of IR sequences[33]. This study supports the idea that longitudinal magnetization evolution depends on both intercompartment exchange and spin-lattice relaxation. To explore this further, the apparent T_1 is an aggregate measurement of T_1 relaxation affecting different water components and pertains to all molecules that exchange fast enough with water. Even in intermediate exchange conditions, the long component of the signals measured from water, once the short component (corresponding mostly to exchange) has decayed, contains a mixed contribution from underlying T_1s from all components. The sequence timing, RF saturation, and exchange processes need to be considered when determining the apparent T_1 and disentangling individual T_1s. Otherwise, different sequences may yield significantly different T_1 estimates.

The proton exchange processes between MW and IEW have been considered in our STAIR-Cones sequence optimization and MWF calculation[24]. Further incorporating MT into the signal modeling may improve the accuracy of MW imaging and our multicompartment modeling.

In summary, like many previous studies, our model does not fully account for biases introduced by MT, diffusion, and other exchange mechanisms that occur between pools, which may affect the accurate estimation of all the PFs. For instance, we did not consider the underestimation of MMPFs within the traditional two-pool MT modeling introduced by on-resonance saturation and dipolar order[39], which will therefore affect the accuracy of our subsequent estimations of MWPF, IEWPF, and FWPF. On the other hand, the proposed simplified multicompartment model may be more robust and easier to translate into clinical practice compared to the complex four-pool MT modeling[33,35]. The MT models with more than three pools are typically limited by their complexity, unreliable parameter estimation, and sensitivity to hardware imperfections and physiological noise, which affect the accurate quantification of the compartments and their exchange effects in in vivo studies. Nevertheless, future studies are necessary to validate and improve our protocol and modeling, considering all potential biases.

There were several limitations in this study. Firstly, manual ROI segmentation was used in this technical feasibility study. For future clinical validation studies with larger cohorts, state-of-the-art methods, such as atlas-based automatic segmentation techniques[62], should be employed for data processing. Secondly, we categorized patients with MS as a homogeneous group without differentiation based on MS subtype (e.g., relapsing-remitting MS or secondary progressive MS) or treatment history. These factors may influence lesion load as well as abnormalities in NAWM and NAGM, and potentially affect comparison of normal and MS brains using WM, GM, and lesion measures[51,63,64]. Additionally, the healthy volunteer group is not age-matched with the MS patient group, and age is a critical factor that can influence quantitative MRI metrics such as T_1 relaxation, MMPF, and brain volume. Therefore, future large cohort studies should recruit patients and controls of similar age. Thirdly, the proposed multicompartment imaging method requires validation, which was not addressed in this technical feasibility study. Thus, the information delivered in this study is largely semi-quantitative. Further validation studies are warranted on this multicompartment imaging protocol. Fourthly, the scan time required for the proposed protocol is relatively long for clinical use (~44 minutes) and will need to be reduced in future studies using techniques such as parallel imaging and compressed sensing[65–67].

5. Conclusion

The multicompartment brain imaging protocol demonstrates the feasibility of mapping the PFs of major tissue components, including MMs, MW, IEW, and FW, in both normal volunteers and patients with MS. The protocol holds significant promise for the assessment of neuroinflammatory and neurodegenerative diseases.

Funding information

Data and code availability statement

The data supporting the reported findings and the code used for analyzing the data are available from the corresponding author upon request.

References

1. Sled JG, Pike GB. Quantitative imaging of magnetization transfer exchange and relaxation properties in vivo using MRI. Magn Reson Med. 2001;46(5):923–931. doi:10.1002/mrm.1278 [PubMed: 11675644]

2. Tozer D, Ramani A, Barker GJ, Davies GR, Miller DH, Tofts PS. Quantitative magnetization transfer mapping of bound protons in multiple sclerosis. Magn Reson Med. 2003;50(1):83–91. doi:10.1002/mrm.10514 [PubMed: 12815682]

3. Alonso-Ortiz E, Levesque IR, Pike GB. MRI-based myelin water imaging: A technical review: MRI-Based Myelin Water Imaging. Magn Reson Med. 2015;73(1):70–81. doi:10.1002/mrm.25198 [PubMed: 24604728]

4. MacKay AL, Laule C. Magnetic Resonance of Myelin Water: An in vivo Marker for Myelin. Zalc B, ed. Brain Plast. 2016;2(1):71–91. doi:10.3233/BPL-160033 [PubMed: 29765849]

5. Jin T, Kim SG. Change of the cerebrospinal fluid volume during brain activation investigated by T1ρ-weighted fMRI. NeuroImage. 2010;51(4):1378–1383. doi:10.1016/j.neuroimage.2010.03.047 [PubMed: 20338251]

6. Qin Q A simple approach for three-dimensional mapping of baseline cerebrospinal fluid volume fraction: 3D CSF Volume Fraction Mapping. Magn Reson Med. 2011;65(2):385–391. doi:10.1002/mrm.22705 [PubMed: 21264932]

7. Bowman FD. Brain Imaging Analysis. Annu Rev Stat Appl. 2014;1(1):61–85. doi:10.1146/annurev-statistics-022513-115611 [PubMed: 25309940]

8. Caviness VS, Makris N, Lange NT, Herbert M, Kennedy DN. Advanced Applications of MRI in Human Brain Science. Keio J Med. 2000;49(2):66–73. doi:10.2302/kjm.49.66 [PubMed: 10900831]

9. Margaret Cheng HL, Stikov N, Ghugre NR, Wright GA. Practical medical applications of quantitative MR relaxometry. J Magn Reson Imaging. 2012;36(4):805–824. doi:10.1002/jmri.23718 [PubMed: 22987758]

10. Suzuki S, Sakai O, Jara H. Combined volumetric T1, T2 and secular-T2 quantitative MRI of the brain: age-related global changes (preliminary results). Magn Reson Imaging. 2006;24(7):877–887. doi:10.1016/j.mri.2006.04.011 [PubMed: 16916705]

11. Brück W, Bitsch A, Kolenda H, Brück Y, Stiefel M, Lassmann H. Inflammatory central nervous system demyelination: Correlation of magnetic resonance imaging findings with lesion pathology: MRI and Pathology of Demyelination. Ann Neurol. 1997;42(5):783–793. doi:10.1002/ana.410420515 [PubMed: 9392578]

12. Filippi M, Rocca MA. MR Imaging of Multiple Sclerosis. Radiology. 2011;259(3):659–681. doi:10.1148/radiol.11101362 [PubMed: 21602503]

13. Yarnykh VL. Fast macromolecular proton fraction mapping from a single off-resonance magnetization transfer measurement. Magn Reson Med. 2012;68(1):166–178. doi:10.1002/mrm.23224 [PubMed: 22190042]

14. Ma YJ, Chang EY, Carl M, Du J. Quantitative magnetization transfer ultrashort echo time imaging using a time-efficient 3D multispoke Cones sequence: 3D Multispoke UTE-Cones-MT Imaging. Magn Reson Med. 2018;79(2):692–700. doi:10.1002/mrm.26716 [PubMed: 28470838]

15. Gurney PT, Hargreaves BA, Nishimura DG. Design and analysis of a practical 3D cones trajectory. Magn Reson Med. 2006;55(3):575–582. doi:10.1002/mrm.20796 [PubMed: 16450366]

16. Ramani A, Dalton C, Miller DH, Tofts PS, Barker GJ. Precise estimate of fundamental in-vivo MT parameters in human brain in clinically feasible times. Magne Reson Imaging. 2002;20(10):721–731. doi:10.1016/S0730-725X(02)00598-2

17. Alizadeh A, Dyck SM, Karimi-Abdolrezaee S. Myelin damage and repair in pathologic CNS: challenges and prospects. Front Mol Neurosci. 2015;8. doi:10.3389/fnmol.2015.00035

18. Oh SH, Bilello M, Schindler M, Markowitz CE, Detre JA, Lee J. Direct visualization of short transverse relaxation time component (ViSTa). NeuroImage. 2013;83:485–492. doi:10.1016/j.neuroimage.2013.06.047 [PubMed: 23796545]

19. Hwang D, Kim DH, Du YP. In vivo multi-slice mapping of myelin water content using T2* decay. NeuroImage. 2010;52(1):198–204. doi:10.1016/j.neuroimage.2010.04.023 [PubMed: 20398770]

20. Du YP, Chu R, Hwang D, et al. Fast multislice mapping of the myelin water fraction using multicompartment analysis of T_2* decay at 3T: A preliminary postmortem study. Magn Reson Med. 2007;58(5):865–870. doi:10.1002/mrm.21409 [PubMed: 17969125]

21. Mackay A, Whittall K, Adler J, Li D, Paty D, Graeb D. In vivo visualization of myelin water in brain by magnetic resonance. Magn Reson Med. 1994;31(6):673–677. doi:10.1002/mrm.1910310614 [PubMed: 8057820]

22. Kim D, Lee HM, Oh SH, Lee J. Probing signal phase in direct visualization of short transverse relaxation time component (ViSTa): ViSTa Phase. Magn Reson Med. 2015;74(2):499–505. doi:10.1002/mrm.25416 [PubMed: 25154599]

23. Bjarnason TA, Vavasour IM, Chia CLL, MacKay AL. Characterization of the NMR behavior of white matter in bovine brain. Magn Reson Med. 2005;54(5):1072–1081. doi:10.1002/mrm.20680 [PubMed: 16200557]

24. Ma Y, Jang H, Lombardi AF, Corey-Bloom J, Bydder GM. Myelin water imaging using a short-TR adiabatic inversion-recovery (STAIR) sequence. Magn Reson Med. 2022;88(3):1156–1169. doi:10.1002/mrm.29287 [PubMed: 35613378]

25. White SJ, Hajnal JV, Young IR, Bydder GM. Use of Fluid-Attenuated Inversion-Recovery Pulse Sequences for Imaging the Spinal Cord. Magn Reson Med. 1992;28(1):153–162. doi:10.1002/mrm.1910280116 [PubMed: 1435218]

26. Sati P, George IC, Shea CD, Gaitán MI, Reich DS. FLAIR*: A Combined MR Contrast Technique for Visualizing White Matter Lesions and Parenchymal Veins. Radiology. 2012;265(3):926–932. doi:10.1148/radiol.12120208 [PubMed: 23074257]

27. Klawiter EC. Current and New Directions in MRI in Multiple Sclerosis: CONTINUUM: Lifelong Learning in Neurology. 2013;19:1058–1073. doi:10.1212/01.CON.0000433283.00221.37 [PubMed: 23917101]

28. Trip SA. Imaging in multiple sclerosis. J Neurol Neurosurg Psych. 2005;76(suppl_3):iii11–iii18. doi:10.1136/jnnp.2005.073213

29. Piechnik SK, Evans J, Bary LH, Wise RG, Jezzard P. Functional changes in CSF volume estimated using measurement of water T_2 relaxation. Magn Reson Med. 2009;61(3):579–586. doi:10.1002/mrm.21897 [PubMed: 19132756]

30. Genovese AV, Hagemeier J, Bergsland N, et al. Atrophied Brain T2 Lesion Volume at MRI Is Associated with Disability Progression and Conversion to Secondary Progressive Multiple Sclerosis. Radiology. 2019;293(2):424–433. doi:10.1148/radiol.2019190306 [PubMed: 31549947]

31. Jakimovski D, Zivadinov R, Weinstock-Guttman B, Bergsland N, Dwyer MG, Lagana MM. Longitudinal analysis of cerebral aqueduct flow measures: multiple sclerosis flow changes driven by brain atrophy. Fluids Barriers CNS. 2020;17(1):9. doi:10.1186/s12987-020-0172-3 [PubMed: 32000809]

32. Öner S, Kahraman AS, Özcan C, et al. Cerebrospinal Fluid Dynamics in Patients with Multiple Sclerosis: The Role of Phase-Contrast MRI in the Differential Diagnosis of Active and Chronic Disease. Korean J Radiol. 2018;19(1):72. doi:10.3348/kjr.2018.19.1.72 [PubMed: 29354002]

33. Manning AP, MacKay AL, Michal CA. Understanding aqueous and non-aqueous proton T1 relaxation in brain. J Magn Reson. 2021;323:106909. doi:10.1016/j.jmr.2020.106909 [PubMed: 33453678]

34. Assländer J, Mao A, Marchetto E, et al. Unconstrained quantitative magnetization transfer imaging: Disentangling T1 of the free and semi-solid spin pools. Imaging Neuroscience. 2024;2:1–16. doi:10.1162/imag_a_00177

35. Weiskopf N, Edwards LJ, Helms G, Mohammadi S, Kirilina E. Quantitative magnetic resonance imaging of brain anatomy and in vivo histology. Nat Rev Phys. 2021;3(8):570–588. doi:10.1038/s42254-021-00326-1

36. Gracien RM, Maiworm M, Brüche N, et al. How stable is quantitative MRI? – Assessment of intra- and inter-scanner-model reproducibility using identical acquisition sequences and data analysis programs. NeuroImage. 2020;207:116364. doi:10.1016/j.neuroimage.2019.116364 [PubMed: 31740340]

37. Preibisch C, Deichmann R. Influence of RF spoiling on the stability and accuracy of T_1 mapping based on spoiled FLASH with varying flip angles. Magn Reson Med. 2009;61(1):125–135. doi:10.1002/mrm.21776 [PubMed: 19097220]

38. Haskell MW, Cauley SF, Bilgic B, et al. Network Accelerated Motion Estimation and Reduction (NAMER): Convolutional neural network guided retrospective motion correction using a separable motion model. Magn Reson Med. 2019;82(4):1452–1461. doi:10.1002/mrm.27771 [PubMed: 31045278]

39. Soustelle L, Troalen T, Hertanu A, et al. Quantitative magnetization transfer MRI unbiased by ON-RESONANCE saturation and dipolar order contributions. Magn Reson Med. 2023;90(3):875–893. doi:10.1002/mrm.29678 [PubMed: 37154400]

40. Ma Y, Zhao W, Wan L, et al. Whole knee joint T_1 values measured in vivo at 3T by combined 3D ultrashort echo time cones actual flip angle and variable flip angle methods. Magn Reson Med. 2019;81(3):1634–1644. doi:10.1002/mrm.27510 [PubMed: 30443925]

41. Ma Y, Carl M, Tang Q, et al. Whole knee joint mapping using a phase modulated UTE adiabatic $T_{1\rho}$ (PM-UTE-ADIAB$T_{1\rho}$) sequence. Magn Reson Med. 2024;91(3):896–910. doi:10.1002/mrm.29871 [PubMed: 37755319]

42. Carl M, Bydder GM, Du J. UTE imaging with simultaneous water and fat signal suppression using a time-efficient multispoke inversion recovery pulse sequence: Optimized Method for Long T2 Signal Suppression. Magn Reson Med. 2016;76(2):577–582. doi:10.1002/mrm.25823 [PubMed: 26309221]

43. Klein S, Staring M, Murphy K, Viergever MA, Pluim J. elastix: A Toolbox for Intensity-Based Medical Image Registration. IEEE Trans Med Imaging. 2010;29(1):196–205. doi:10.1109/TMI.2009.2035616 [PubMed: 19923044]

44. Rauf A, Badoni H, Abu-Izneid T, et al. Neuroinflammatory Markers: Key Indicators in the Pathology of Neurodegenerative Diseases. Molecules. 2022;27(10):3194. doi:10.3390/molecules27103194 [PubMed: 35630670]

45. Mayer AR, Ling JM, Dodd AB, et al. Multicompartmental models and diffusion abnormalities in paediatric mild traumatic brain injury. Brain. 2022;145(11):4124–4137. doi:10.1093/brain/awac221 [PubMed: 35727944]

46. Miller DH, Thompson AJ, Filippi M. Magnetic resonance studies of abnormalities in the normal appearing white matter and grey matter in multiple sclerosis. J Neurol. 2003;250(12):1407–1419. doi:10.1007/s00415-003-0243-9 [PubMed: 14673572]

47. Noseworthy JH, Lucchinetti C, Rodriguez M, Weinshenker BG. Multiple Sclerosis. N Engl J Med. 2000;343(13):938–952. doi:10.1056/NEJM200009283431307 [PubMed: 11006371]

48. Sherafat A, Pfeiffer F, Nishiyama A. Shaping of Regional Differences in Oligodendrocyte Dynamics by Regional Heterogeneity of the Pericellular Microenvironment. Front Cell Neurosci. 2021;15:721376. doi:10.3389/fncel.2021.721376 [PubMed: 34690700]

49. Dwyer MG, Bergsland N, Ramasamy DP, Jakimovski D, Weinstock-Guttman B, Zivadinov R. Atrophied Brain Lesion Volume: A New Imaging Biomarker in Multiple Sclerosis. J Neuroimaging. 2018;28(5):490–495. doi:10.1111/jon.12527 [PubMed: 29856910]

50. Zivadinov R, Bergsland N, Dwyer MG. Atrophied brain lesion volume, a magnetic resonance imaging biomarker for monitoring neurodegenerative changes in multiple sclerosis. Quant Imaging Med Surg. 2018;8(10):979–983. doi:10.21037/qims.2018.11.01 [PubMed: 30598875]

51. Newbould RD, Nicholas R, Thomas CL, et al. Age independently affects myelin integrity as detected by magnetization transfer magnetic resonance imaging in multiple sclerosis. NeuroImage: Clinical. 2014;4:641–648. doi:10.1016/j.nicl.2014.02.004 [PubMed: 24936415]

52. Lassmann H Pathogenic Mechanisms Associated With Different Clinical Courses of Multiple Sclerosis. Front Immunol. 2019;9:3116. doi:10.3389/fimmu.2018.03116 [PubMed: 30687321]

53. Rahmanzadeh R, Lu PJ, Barakovic M, et al. Myelin and axon pathology in multiple sclerosis assessed by myelin water and multi-shell diffusion imaging. Brain. 2021;144(6):1684–1696. doi:10.1093/brain/awab088 [PubMed: 33693571]

54. Yarnykh VL, Bowen JD, Samsonov A, et al. Fast Whole-Brain Three-dimensional Macromolecular Proton Fraction Mapping in Multiple Sclerosis. Radiology. 2015;274(1):210–220. doi:10.1148/radiol.14140528 [PubMed: 25208343]

55. Laule C, Vavasour IM, Moore GRW, et al. Water content and myelin water fraction in multiple sclerosis. J Neurology. 2004;251(3):284–293. doi:10.1007/s00415-004-0306-6

56. Oh J, Han ET, Lee MC, Nelson SJ, Pelletier D. Multislice Brain Myelin Water Fractions at 3T in Multiple Sclerosis. J Neuroimaging. 2007;17(2):156–163. doi:10.1111/j.1552-6569.2007.00098.x [PubMed: 17441837]

57. Ge Y, Grossman RI, Udupa JK, Babb JS, Kolson DL, McGowan JC. Magnetization transfer ratio histogram analysis of gray matter in relapsing-remitting multiple sclerosis. AJNR Am J Neuroradiol. 2001;22(3):470–475. [PubMed: 11237968]

58. Bozzali M, Cercignani M, Sormani MP, Comi G, Filippi M. Quantification of brain gray matter damage in different MS phenotypes by use of diffusion tensor MR imaging. AJNR Am J Neuroradiol. 2002;23(6):985–988. [PubMed: 12063230]

59. Henkelman RM, Stanisz GJ, Graham SJ. Magnetization transfer in MRI: a review. NMR in Biomedicine. 2001;14(2):57–64. doi:10.1002/nbm.683 [PubMed: 11320533]

60. Yarnykh VL, Kisel AA, Khodanovich MY. Scan–Rescan Repeatability and Impact of B_0 and B_1 Field Nonuniformity Corrections in Single-Point Whole-Brain Macromolecular Proton Fraction Mapping. Magn Reson Imaging. 2020;51(6):1789–1798. doi:10.1002/jmri.26998

61. Sled JG, Pike GB. Quantitative Interpretation of Magnetization Transfer in Spoiled Gradient Echo MRI Sequences. J Magn Reson. 2000;145(1):24–36. doi:10.1006/jmre.2000.2059 [PubMed: 10873494]

62. Cabezas M, Oliver A, Lladó X, Freixenet J, Bach Cuadra M. A review of atlas-based segmentation for magnetic resonance brain images. Computer Methods and Programs in Biomedicine. 2011;104(3):e158–e177. doi:10.1016/j.cmpb.2011.07.015 [PubMed: 21871688]

63. Antel J, Antel S, Caramanos Z, Arnold DL, Kuhlmann T. Primary progressive multiple sclerosis: part of the MS disease spectrum or separate disease entity? Acta Neuropathol. 2012;123(5):627–638. doi:10.1007/s00401-012-0953-0 [PubMed: 22327362]

64. Cunill V, Massot M, Clemente A, et al. Relapsing–Remitting Multiple Sclerosis Is Characterized by a T Follicular Cell Pro-Inflammatory Shift, Reverted by Dimethyl Fumarate Treatment. Front Immunol. 2018;9:1097. doi:10.3389/fimmu.2018.01097 [PubMed: 29896193]

65. Ma YJ, Searleman AC, Jang H, et al. Whole-Brain Myelin Imaging Using 3D Double-Echo Sliding Inversion Recovery Ultrashort Echo Time (DESIRE UTE) MRI. Radiology. 2020;294(2):362–374. doi:10.1148/radiol.2019190911 [PubMed: 31746689]

66. Athertya JS, Ma Y, Masoud Afsahi A, et al. Accelerated Quantitative 3D UTE-Cones Imaging Using Compressed Sensing. Sensors. 2022;22(19):7459. doi:10.3390/s22197459 [PubMed: 36236557]

67. Lustig M, Donoho D, Pauly JM. Sparse MRI: The application of compressed sensing for rapid MR imaging. Magn Reson Med. 2007;58(6):1182–1195. doi:10.1002/mrm.21391 [PubMed: 17969013]
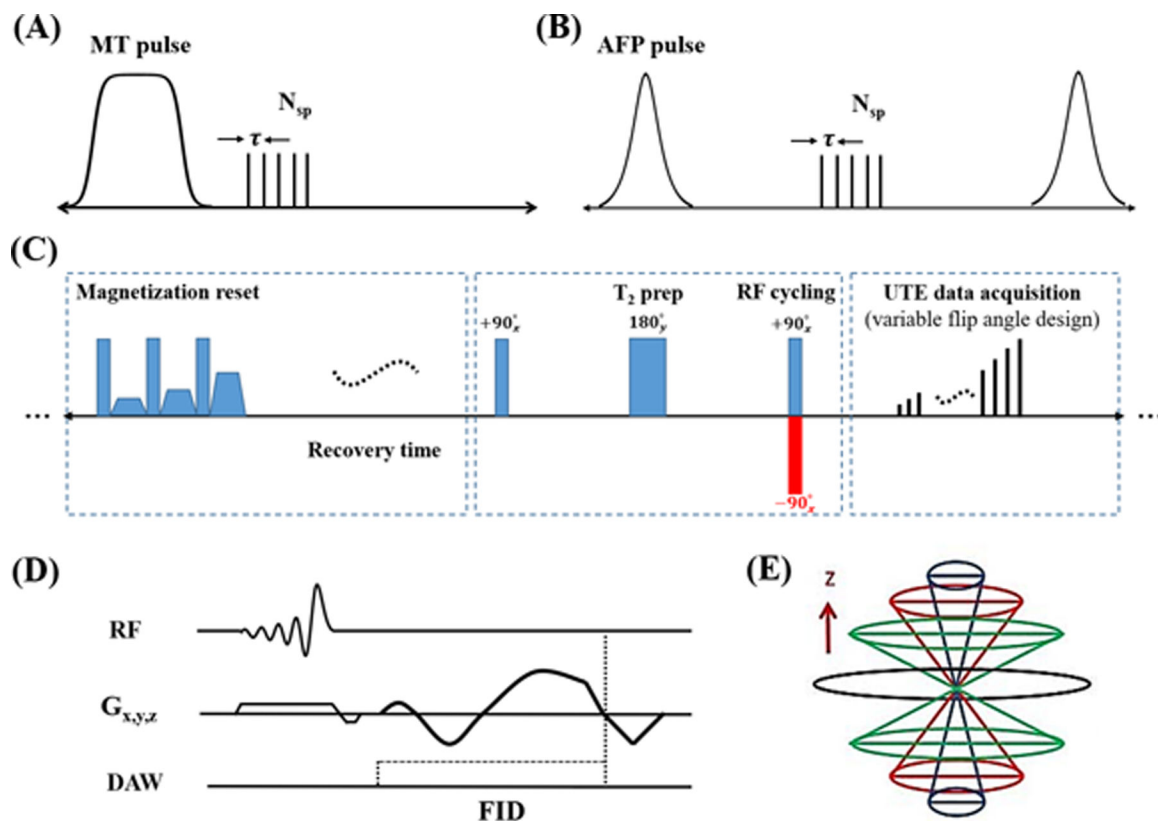
Figure 1.
Sequence diagrams for the proposed protocol: (A) magnetization transfer prepared Cones (MT-Cones) sequence for two-pool MT modeling; (B) short repetition time adiabatic inversion recovery prepared Cones (STAIR-Cones) sequence for selective MW imaging; (C) highly T_2w-Cones with a long free decay time (e.g., 350 ms) in the T_2 preparation module for selective FW imaging; (D) PDw-Cones for TW imaging. 3D Cones data sampling strategy is employed for all the sequences (E).
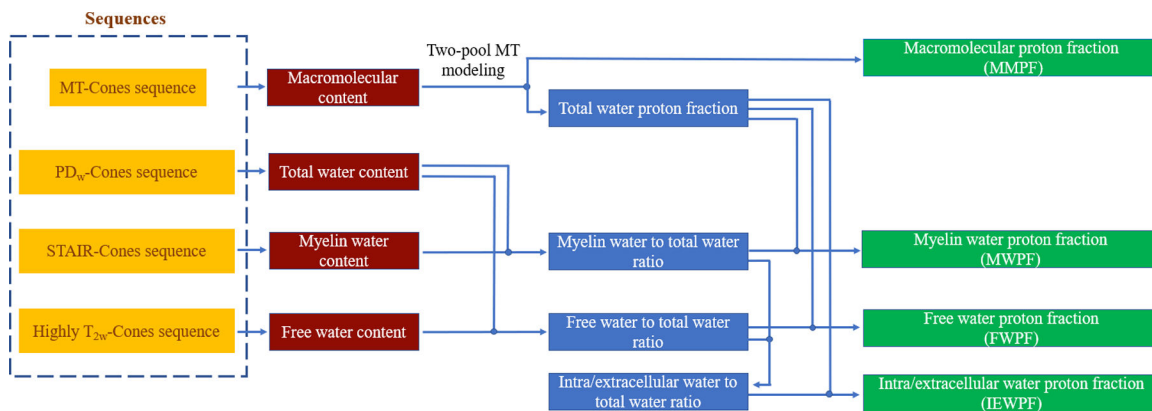
Figure 2.
Workflow to map PFs of brain macromolecules (MM), MW, IEW, and FW. Four different types of Cones sequences (i.e., MT-, PDw-, STAIR- and highly T_2w-) are included. MMPF and TWPF are first estimated by two-pool MT modeling. The ratios of MW, FW and IEW to TW are calculated using Eq. [1]. With known MMPF estimated by MT modeling, TWPPF can be easily calculated by 1-MMPF. Then MWPF, IEWPF, and FWPF are obtained by Eqs. [3]–[5]. Yellow boxes show data acquisition sequences. Brown boxes show imaged brain compartments. Blue boxes show intermediate results, including the TW PF and water signal ratios. Green boxes show the final PF maps.
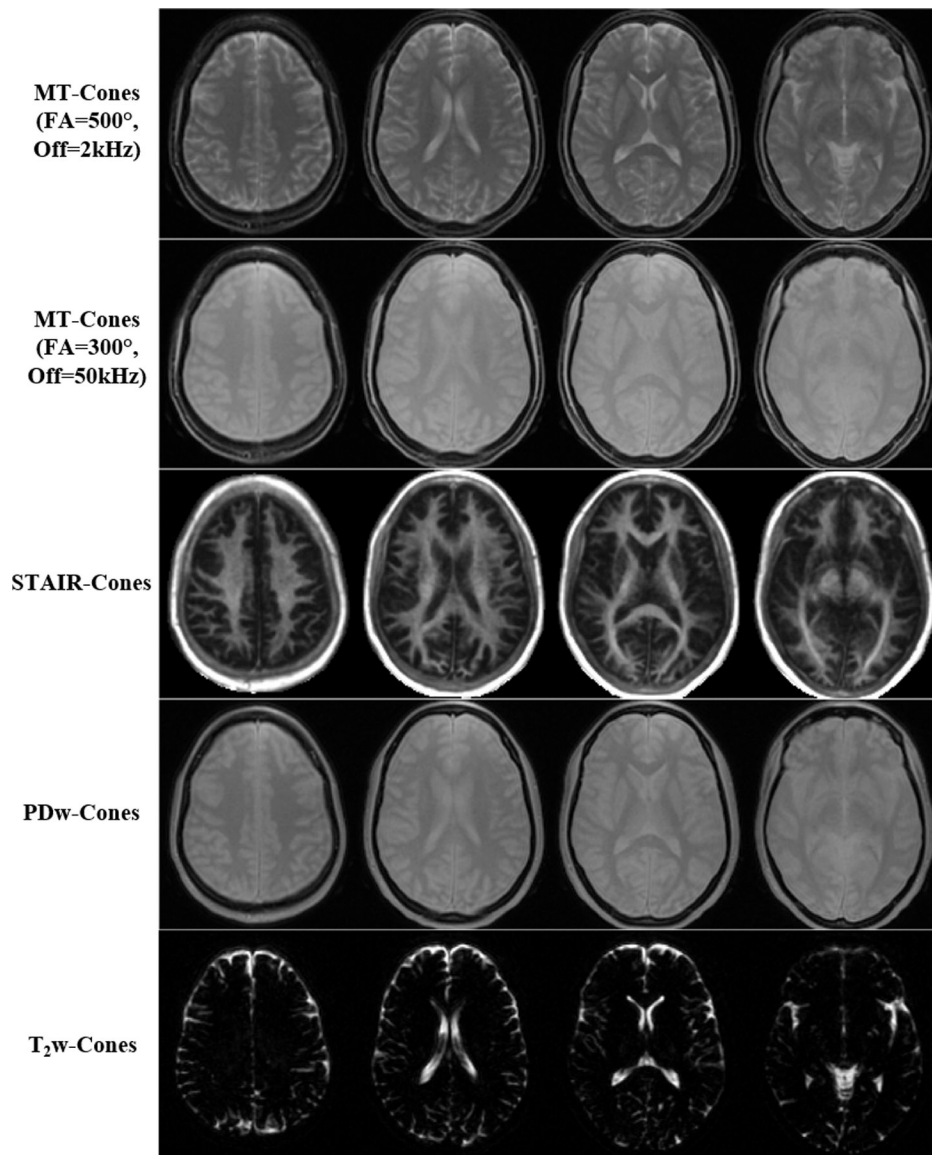
Figure 3.
Representative images acquired with the MT-, PDw-, STAIR- and highly T_2w-Cones sequences from a normal volunteer (30-year-old, female). Images with a higher MT FA (500° vs. 300°) and a smaller frequency offset (2kHz vs. 50kHz) show a stronger MT effect (first two rows). As can be seen from the STAIR-Cones images (third row), the WM region has a much higher MW and myelin content than the GM region. FW is selectively imaged by the highly T_2w-Cones sequence (fifth row), when signals from all the other compartments are completely decayed.
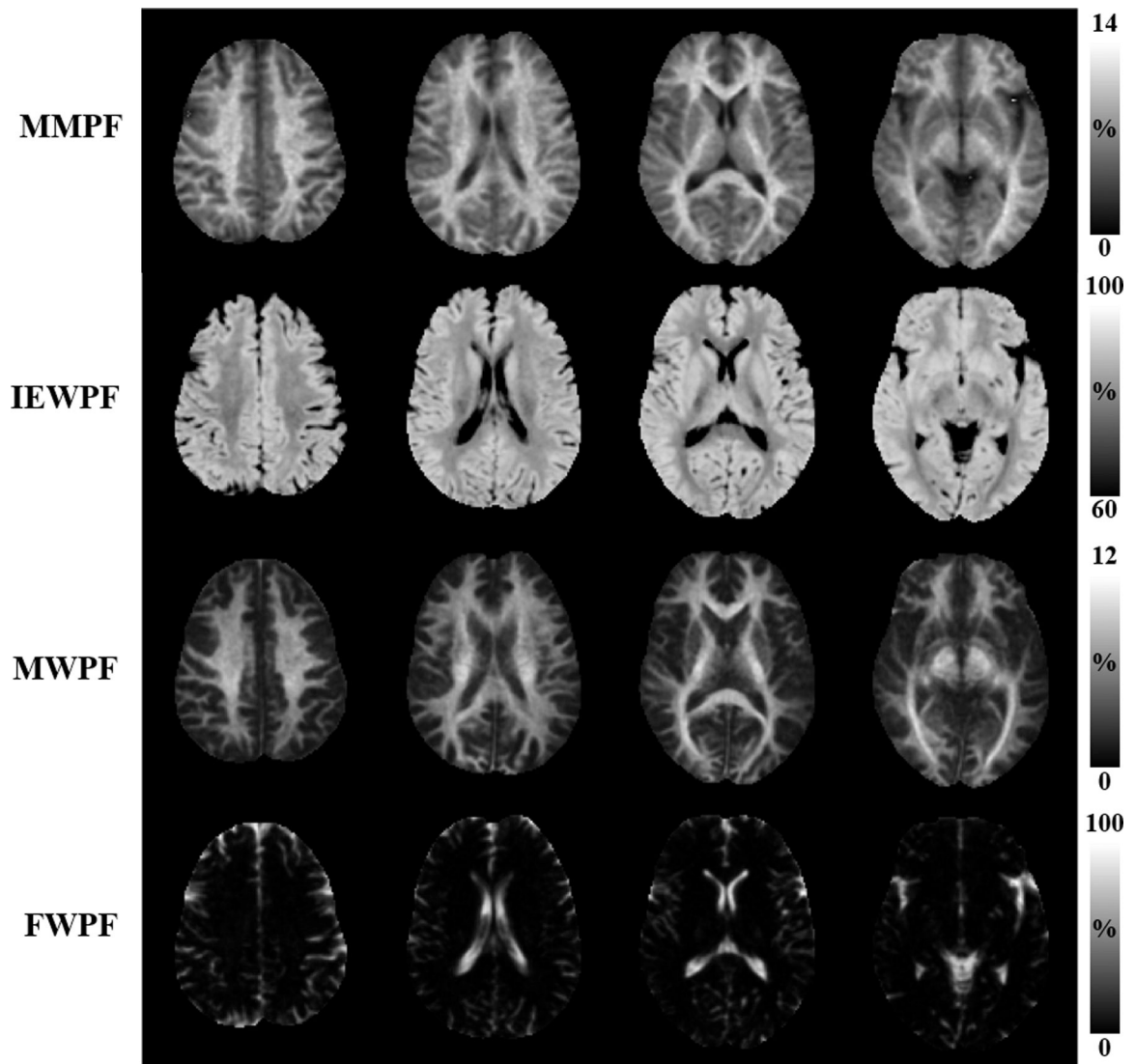
Figure 4.
Representative brain multicompartment maps of the same 30-year-old normal volunteer as in Figure 3, including MMPF (first row), IEWPF (second row), MWPF (third row), and FWPF (fourth row), estimated using the methods described in Figure 2. As can be seen, white matter has much higher MMPF and MWPF values than grey matter, while grey matter has a higher IEWPF value than white matter. FW is seen in non-white and grey matter regions such as the ventricles and subarachnoid space.
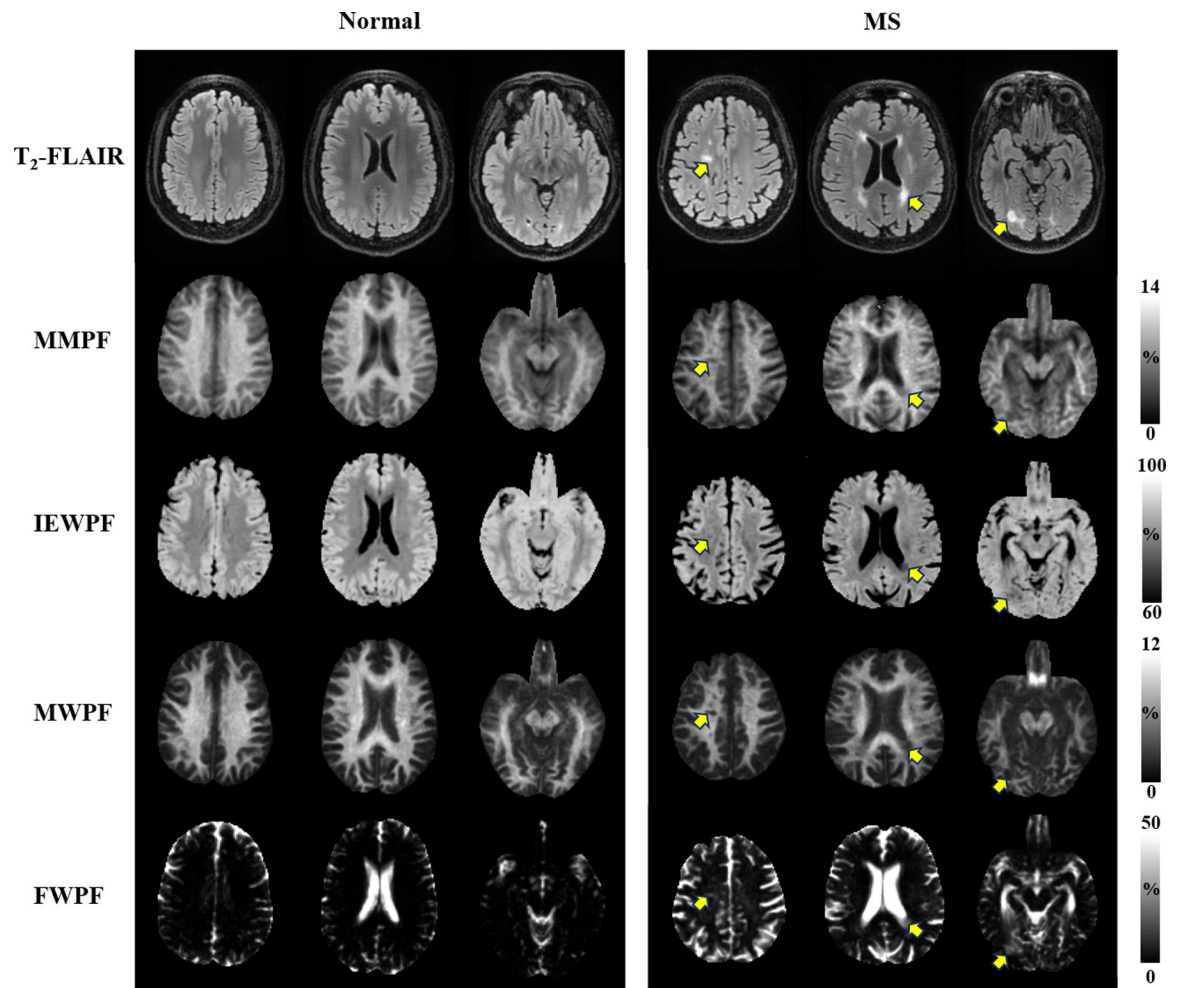
Figure 5.
MMPF, MWPF, IEWPF, and FWPF mapping comparison between a 26-year-old normal volunteer (left panel) and three MS patients of ages 68, 63, and 58 years from first to third columns in the right panel. T_2-FLAIR images are displayed in the first row of both panels for lesion localization. Lesions in the MS patients are shown by the yellow arrows.
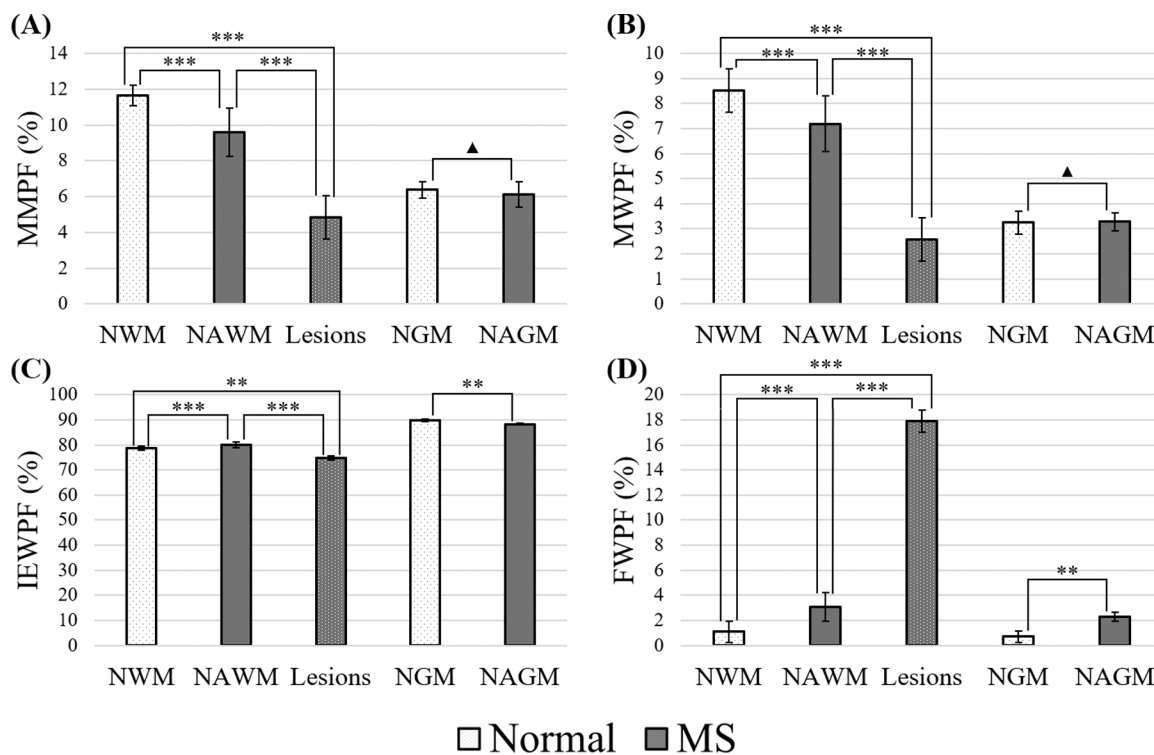
Figure 6.
Bar plots of the averaged MMPF, MWPF, IEWPF, and FWPF values of NWM/NAWM, NGM/NAGM, and lesions from the ten normal volunteers and the five patients with MS. Independent t-test analysis was performed to investigate statistical differences of all the PF measurements between NWM and NAWM, between NWM and lesions, between NAWM and lesions, and between NGM and NAGM ("***" indicates $p<0.001$, "**" indicates $p<0.05$, and "▲" indicates $p>0.05$). NWM and NGM bars from the normal volunteers are depicted in dotted white. NAWM and NAGM bars from the patients with MS are depicted in grey and the Lesions bar is depicted in dotted grey.

Table 1

Detailed scan parameters of the comprehensive MR imaging protocol.

3D MT-Cones (Two-pool MT modeling)	3D PDw-Cones (Total water imaging)	3D STAIR-Cones (Myelin water imaging)
FOV = 22×22×14.4 cm^3, voxel size = 1.38×1.38×4 mm^3, TR/TE = 48.6/0.8 ms, N_{sp} = 5, τ = 5.7 ms, FA = 5°, bandwidth = 83.3 kHz, 10 scans with two different MT FAs (i.e., 500° and 300°) and five different frequency offsets (i.e., 2, 5, 10, 20 and 50 kHz), total scan time = 15min	FOV = 22×22×14.4 cm^3, voxel size = 1.38×1.38×4 mm^3, TR/TE = 7/2 ms, FA = 1°, bandwidth = 83.3 kHz, scan time = 1 min 34s	FOV = 22×22×14.4 cm^3, voxel size = 1.38×1.38×4 mm^3, TR/TI = 250/114 ms, TE = 2 ms, N_{sp} = 5, τ = 5.4 ms, FA = 40°, bandwidth = 83.3 kHz, scan time = 10 min
3D Highly T$_2$w-Cones (Free water imaging)	**3D VFA-Cones (T$_1$ mapping)**	**3D AFI-Cones (B$_1$ mapping)**
FOV = 22×22×14.4 cm^3, voxel size = 1.38×1.38×4 mm^3, TR/TE = 1420/0.8 ms, T$_2$ preparation time= 350 ms, τ = 5.7 ms, FA of the last excitation = 60°, bandwidth = 62.5 kHz, scan time = 7 min	FOV = 22×22×14.4 cm^3, voxel size = 1.38×1.38×4 mm^3, TR/TE = 7.6/0.8 ms, FAs = 2°, 4°, 8°, 12°, 16°, bandwidth = 83.3 kHz, scan time = 5 min	FOV = 22×22×14.4 cm^3, voxel size = 4.58×4.58×8 mm^3, TR$_1$/TR$_2$ = 20/100 ms, TE = 0.8 ms, FA = 45°, bandwidth = 125 kHz, scan time = 2 min 37s

Table 2

Summarized measurements of MMPF, MWPF, IEWPF, and FWPF (mean ± SD) in eight NWM/NAWM regions: G (genu) LCS (left centrum semiovale), LS (left subcortical WM), LV (left periventricular region), RCS (right centrum semiovale), RS (right subcortical WM), RV (right periventricular region), S (splenium), two NGM/NAGM regions: P (putamen), T (thalamus), and lesions in ten normal volunteers and five patients with MS.

		Normal						MS			
		MMPF (%)	MWPF (%)	IEWPF (%)	FWPF (%)			MMPF (%)	MWPF (%)	IEWPF (%)	FWPF (%)
NWM	G	12.1 ± 0.5	9.2 ± 1.2	76.2 ± 1	2.5 ± 0.9	NAWM	G	9.5 ± 1.4	7.7 ± 0.7	79.8 ± 1.7	2.9 ± 1.1
	LCS	11.4 ± 0.5	7.7 ± 0.4	79.9 ± 0.7	0.9 ± 0.3		LCS	9.1 ± 0.8	6.3 ± 0.7	79.1 ± 0.6	5.5 ± 1
	LS	11.8 ± 0.6	8.1 ± 0.5	79.6 ± 1.1	0.5 ± 0.3		LS	9.9 ± 0.9	7.2 ± 0.7	81.7 ± 0.6	1.2 ± 0.6
	LV	11.4 ± 0.5	8.4 ± 0.4	79.4 ± 0.6	0.8 ± 0.2		LV	10.3 ± 1	7.5 ± 0.5	80.2 ± 0.6	2 ± 0.7
	RCS	11.3 ± 0.5	8 ± 0.4	79.6 ± 0.7	1.2 ± 0.3		RCS	8.4 ± 1.5	6.2 ± 0.5	78.8 ± 1.1	6.5 ± 2.3
	RS	12.1 ± 0.4	8.3 ± 0.6	79.2 ± 0.9	0.5 ± 0.3		RS	10.2 ± 1.4	6.8 ± 1	81.6 ± 2.1	1.3 ± 0.4
	RV	11.4 ± 0.6	8.8 ± 0.3	79 ± 0.8	0.7 ± 0.3		RV	9.9 ± 1.6	7.3 ± 1.4	80.9 ± 2.9	1.9 ± 1
	S	11.6 ± 0.4	9.7 ± 0.5	77 ± 0.9	1.6 ± 0.7		S	9.5 ± 1.9	8.5 ± 1.6	78.8 ± 2.4	3.2 ± 1.4
	Avg	**11.6 ± 0.6**	**8.5 ± 0.9**	**78.7 ± 1.5**	**1.1 ± 0.8**		**Avg**	**9.6 ± 1.4**	**7.2 ± 1.1**	**80.1 ± 1.9**	**3.1 ± 2.1**
						Lesion	**Avg**	**4.8 ± 1.2**	**2.6 ± 0.9**	**74.7 ± 4**	**18.4 ± 4.2**
NGM	P	6 ± 0.3	3.1 ± 0.2	90.3 ± 0.4	0.5 ± 0.2	NAGM	P	6 ± 0.8	3.4 ± 0.3	89.5 ± 0.7	1 ± 0.6
	T	6.7 ± 0.3	3.4 ± 0.6	89.1 ± 0.8	0.9 ± 0.4		T	6.2 ± 0.7	3.1 ± 0.4	87.1 ± 1.5	3.6 ± 0.7
	Avg	**6.4 ± 0.5**	**3.2 ± 0.5**	**89.7 ± 0.9**	**0.7 ± 0.4**		**Avg**	**6.1 ± 0.7**	**3.3 ± 0.4**	**88.3 ± 1.6**	**2.3 ± 1.4**